Frontiers of Materials Science

Electronic Supplementary Material

Dual-crosslinked and dual-networked hydrogels with high mechanical properties for cost-effective solar water desalination and purification

Shukun Guo[1], Wenxin Wang[1], Ruizhi Wang[1], Yang Chen[3], Ning Wang (✉)[1], Martin Jensen[2], and Xianfeng Li[1]

1 State Key Laboratory of Separation Membranes and Membrane Processes, Tianjin Municipal Key Lab of Advanced Energy Storage Material and Devices, School of Material Science and Engineering, Tiangong University, Tianjin 300387, China
2 Department of Chemistry and Bioscience, Aalborg University, DK-9220 Aalborg, Denmark
3 Shandong Dongyue Future Hydrogen Energy Materials Co., Ltd., Zibo 256401, China

E-mail: wangntjpu@hotmail.com

1 Experimental materials and equipment

Reagents in this work were purchased, including potassium ferricyanide trihydrate (chemically pure) from Shanghai Boer Chemical Reagent Co., Ltd., ferric chloride hexahydrate from Tianjin Kemiou Chemical Reagent Co., Ltd., cellulose cotton staple (industrial grade) from Tangshan Sanyou Group Xingda Chemical Fiber Co., Ltd., sodium alginate (CMC) from Shanghai Tengzhun Biotechnology Co., Ltd., urea from China National Pharmaceutical Group Chemical Reagent Co., Ltd., epichlorohydrin (ECH) from Tianjin Hynes Biochemical Technology Co., Ltd., sodium hydroxide (NaOH) and anhydrous ethanol from Tianjin Windship Chemical Reagent Technology Co., Ltd., while methylene blue (MB), methyl orange (MO), rhodamine B (RhB), and crystallized calcium chloride ($CaCl_2$) were from Tianjin Guangfu Technology Development Co., Ltd. Except for some materials specially labeled, all reagents are of analytical grade that require no further purification before use.

The indoor water evaporation device is shown in Fig. S1.

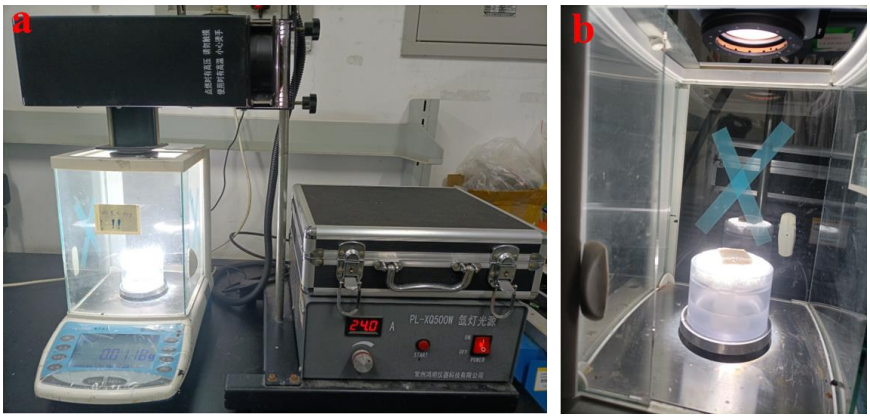

Fig. S1 Photos of the indoor water evaporation device.

2 Preparation of Fe-MOF-derived nanoparticles

The preparation process of Fe-MOF-derived nanoparticles (NPs) are as follows [1]: 8.44 g of $K_4Fe(CN)_6 \cdot 3H_2O$ was dissolved in 100 mL of deionized water under continuous stirring for the formation of Solution A. 2.7 g of $FeCl_3 \cdot 6H_2O$ was dissolved in 100 mL of deionized water with continuous stirring to form Solution B. Subsequently, Solution B was slowly added into Solution A to form a dark blue precipitate. The mixed solution was then stirred vigorously for 1 h. After vacuum filtration of the mixed solution, the precipitated fine particles were collected, washed three to five times with water and ethanol separately, and dried under vacuum at 80 ℃ for 24 h. Finally, Fe-MOF NPs were obtained through annealing them followed by carbonization at 500 ℃ under nitrogen atmosphere for 2 h.

3 Supporting analysis methods and figures

Figure S2(a) shows water contact angles of CECH hydrogels with different contents of the crosslinker, from which it is seen that the CECH-5 dry gel has the best hydrophilic performance, and the water droplets instantly disappear on the surface. On the contrary, other hydrogels still show higher contact angles after 3 s, demonstrating their inferior water transport abilities. Figure S2(b) shows relationships between the swelling capacity and the time for differently prepared CECH hydrogels. The swelling capacities of all samples increase rapidly in the initial 30 min, which is due to the osmotic pressure that will continue to swell the polymer chains to promote the water absorption of the hydrogel [2]. After about 60 min, the equilibrium is reached as the crosslinking agent prevents the hydrogel from dissolving. The CECH-5 hydrogel exhibits the highest water absorption of 34.7 $g \cdot g^{-1}$. When the ECH content is lower, the water contents of CECH-3 and CECH-4 hydrogels are 23.6 and 25.0 $g \cdot g^{-1}$, respectively, attributed to the insufficient crosslinking to support the network structure of the hydrogel. Similarly, the water saturation levels of CECH-6 and CECH-7 hydrogels decrease to 19.8 and 6.0 $g \cdot g^{-1}$, respectively, attributed to the further reaction between cellulose hydroxyl and ECH epoxy groups, the increase in the crosslinking density, the formation of spatial site-blocking effect, and the decrease in the amount of hydrophilic −OH.

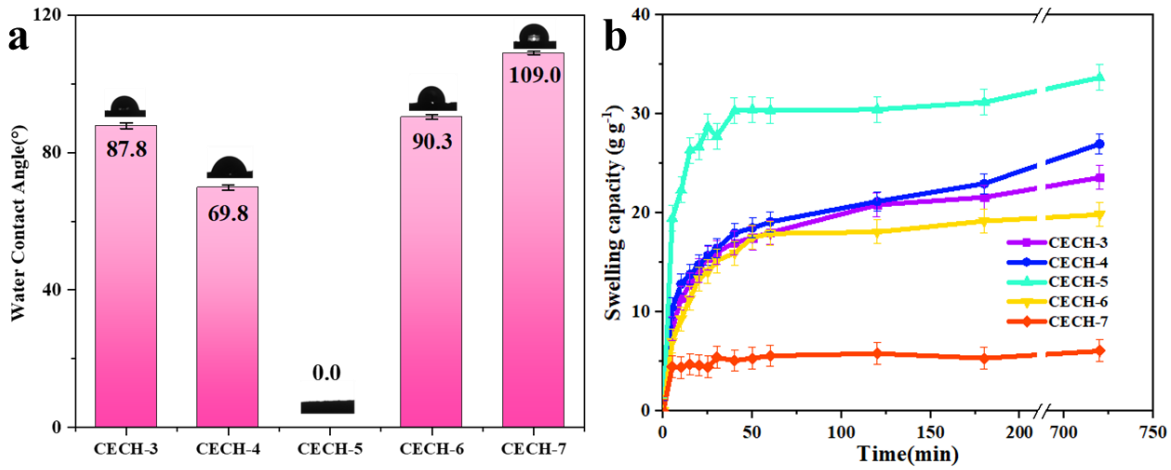

Fig. S2 Performances of CECH hydrogels containing the crosslinker (ECH) with different contents: **(a)** water contact angles over 3 s; **(b)** time-dependent swelling behaviors.

Fe-MOF-derived NPs are produced through the combination of Fe_3O_4 and Fe_3C. As shown in Fig. S3(a), the diffraction peaks located at 30.2°, 35.5°, 43.2°, 57.1°, and 62.7° correspond to (2 2 0), (3 1 1), (4 0 0), (5 1 1), and (4 4 0) crystal planes, which match with a mixture of ferric and ferrous oxide, Fe_3O_4 (JCPDS No. 88-0315); the diffraction peaks located at 40.6°, 43.8°, 45°, and 45.9° diffraction peaks are attributed to (2 0 1), (1 0 2), (0 3 1), and (1 1 2) crystal planes of Fe_3C (JCPDS No. 72-1110) [1]. The above results confirm the successful preparation of Fe-MOF NPs. The elemental composition and bond group distribution of cellulose, SA and CSHs hybrid hydrogels are analyzed by XPS through the C 1s of C−C bond (284.8 eV) as shown in Figs. S3(b)–S3(d). The central peak of CSH-0 located at 284.8 eV (28.3%) was higher than those of cellulose (26.94%) and SA (22.03%), proving the successful chemical crosslinking of ECH cellulose and SA in the formation of more C−C bonds [3]. The equivalent enthalpy of evaporation for water in the hydrogel can be estimated by placing pure water and hydrogel of the same surface area in a dark container containing a supersaturated potassium carbonate solution for 1 h. Since they are simultaneously under the same energy input, the equivalent enthalpy of evaporation of water in the hydrogel can be estimated according to Eq. (S1) as follows [4]:

$$U_{\text{in}} = E_0 m_0 = E_{\text{equ}} m_{\text{g}} \tag{S1}$$

where m_0 and m_g denote mass changes (unit: g) of pure water and the hydrogel sample under dark conditions, respectively, and E_0 is the enthalpy (unit: $J \cdot g^{-1}$) of evaporation for pure water under dark conditions.

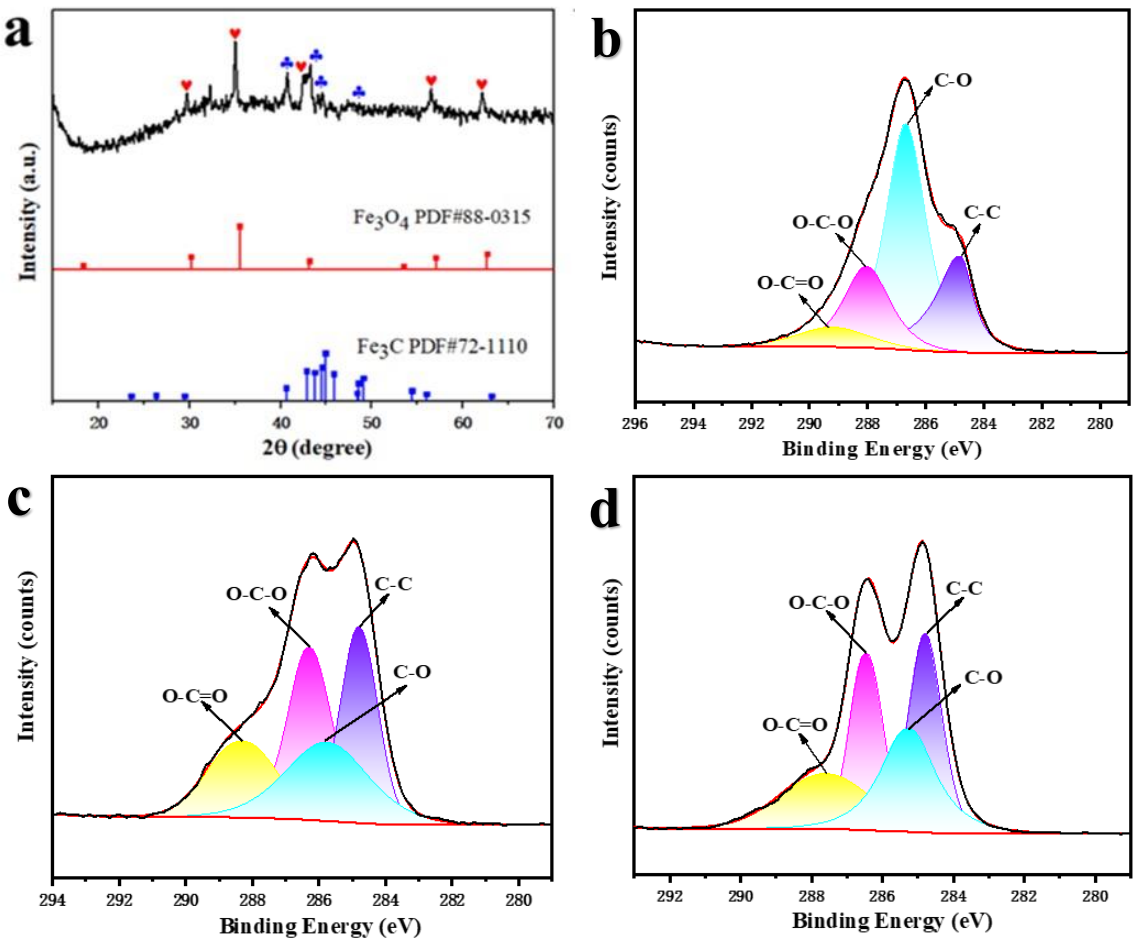

Fig. S3 (a) XRD pattern of Fe-MOF derived nanoparticles. **(b)(c)(d)** High-resolution C 1s XPS spectra of cellulose (Panel (b)), SA (Panel (c)), and CSH-0 (Panel (d)) hybrid hydrogels.

Table S1 Viscosities of C_iS_jH hydrogels with different matrix ratios

C_iS_jH hydrogel	Mass of basic content/g		Value		Viscosity/(mPa·s)
	Cellulose	SA	*i*	*j*	
$C_{0.5}S_{0.5}H$	0.5	0.5	0.5	0.5	176.98 ± 12.07
$C_{0.5}S_1H$	0.5	1.0	0.5	1	455.27 ± 8.8
$C_{0.5}S_{1.5}H$	0.5	1.5	0.5	1.5	715.53 ± 3.58
$C_1S_{0.5}H$	1.0	0.5	1	0.5	627.52 ± 19.26
C_1S_1H	1.0	1.0	1	1	1065.96 ± 9.07
$C_1S_{1.5}H$	1.0	1.5	1	1.5	2527.71 ± 20.99
C_1S_2H	1.0	2.0	1	2	8525.01 ± 88.57
$C_{1.5}S_{0.5}H$	1.5	0.5	1.5	0.5	2337.73 ± 21.22
$C_{1.5}S_1H$	1.5	1.0	1.5	1	4274.04 ± 24.05
$C_2S_{0.5}H$	2.0	0.5	2	0.5	7542.64 ± 63.85

Table S2 EDS elemental analysis results of the CSH-4 hybridized hydrogel before and after the Ca^{2+} crosslinking control

Hydrogel	*c*(C)/wt.%	*c*(O)/wt.%	*c*(Ca)/wt.%	*c*(Fe)/wt.%	*c*(Cl)/wt.%	*c*(Na)/wt.%
CSH′-4	48.99	43.70	0.00	3.16	1.80	2.35
CSH-4	47.49	43.93	2.69	5.27	0.26	0.36

Table S3 Equivalent enthalpies of evaporation for pure water and different hydrogel samples

Sample	E_{equ}/(J·g^{-1})
Purified water	2442
CSH-4	1276
CSH-0	1711
CG	1849

Table S4 Comparison of evaporation performance of solar photovoltaic evaporators under one solar radiation condition in recent reports [4–18]

Material	Solar absorptivity/%	Evaporation rate/(kg·m^{-2}·h^{-1})	Energy efficiency/%	Ref.
CNT/SLS/PVA hydrogel	95	2.09	–	[4]
NHrG membrane	90	1.85	95.4	[5]
A-RGO/MX	97	2.09	93.5	[6]
Starch–polyacrylamide	–	1.79	–	[7]
(P(AM-co-AA))/CB	–	2.42	92.8	[8]
CNT/CNC/PDMS	–	1.35	87.4	[9]
MnO_2/CS hydrogel	94	1.78	90.6	[10]
CNT/Starch hydrogel	92	2.77	88	[11]
Mn-MOF cotton cloth	97	2.38	98.4	[12]
PPy/CNC membrane	–	1.96	88.92	[13]
(MXene/LSC) (PVA/CS) hydrogel	94	2.73	92.3	[14]
PVA/rGO hydrogel	97	1.65	87	[15]
CNTs-PAAm hydroge	99.45	1.82	–	[16]
Ti_4O_7-PVA hydrogel	99.56	4.45	90.69	[17]
PEG@APL/T-Loofah	–	1.75	97.6	[18]
Fe-MOF/cellulose/SA hydrogel	97	2.52	89.32	This work

In order to investigate the purification ability of the CSH-4 hybridized hydrogel for seawater and printing and dyeing wastewater, we conducted an experiment on evaporation under outdoor sunlight. As shown in Fig. S4, outdoor temperatures and solar irradiance are at their highest at 12:00 pm.

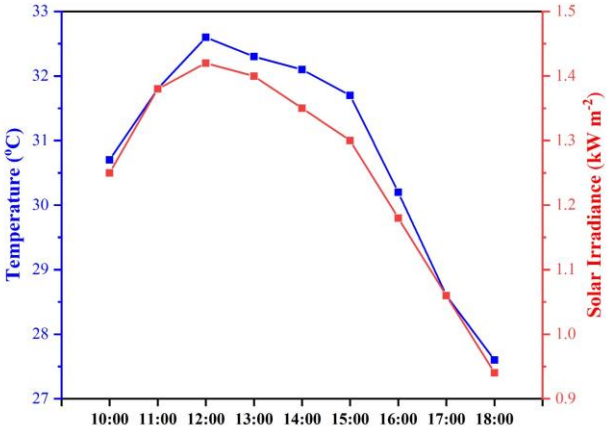

Fig. S4 Outdoor temperature change and solar irradiance change curves.

References

[1] Guo Y, Lu H, Zhao F, et al. Biomass-derived hybrid hydrogel evaporators for cost-effective solar water purification. Advanced Materials, 2020, 32(11): e1907061

[2] Nguyen M N, Tran T T, Nguyen Q T, et al. Simple synthesis of cellulose hydrogels based on the direct dissolution of cellulose in tetrabutylphosphonium hydroxide followed by crosslinking. Polymers for Advanced Technologies, 2022, 33(10): 3376–3385

[3] Chen X, Chen C, Zhu J. Facile preparation of cellulose-attapulgite nanocomposite hydrogel for dye adsorption. Iranian Polymer Journal, 2019, 28(4): 347–359

[4] Hao L, Liu N, Bai H, et al. High-performance solar-driven interfacial evaporation through molecular design of antibacterial, biomass-derived hydrogels. Journal of Colloid and Interface Science, 2022, 608(1): 840–852

[5] Zang L L, Sun L G, Zhang S C, et al. Nanofibrous hydrogel-reduced graphene oxide membranes for effective solar-driven interfacial evaporation and desalination. Chemical Engineering Journal, 2021, 422: 129998

[6] Li W, Li X F, Chang W, et al. Vertically aligned reduced graphene oxide/Ti_3C_2Tx MXene hybrid hydrogel for highly efficient solar steam generation. Nano Research, 2020, 13(11): 3048–3056

[7] Mu X J, Zhou J H, Wang P F, et al. A robust starch–polyacrylamide hydrogel with scavenging energy harvesting capacity for efficient solar thermoelectricity–freshwater cogeneration. Energy & Environmental Science, 2022, 15(8): 3388–3399

[8] Liang Y Z, Bai Y T, Mao J, et al. Solar-initiated frontal polymerization of photothermic hydrogels with high swelling properties for efficient water evaporation. Solar RRL, 2022, 6(2): 2100919

[9] Zhu L L, Ding T P, Gao M M, et al. Shape conformal and thermal insulative organic solar absorber sponge for photothermal water evaporation and thermoelectric power generation. Advanced Energy Materials, 2019, 9: 1900250

[10] Irshad M S, Wang X, Abbasi M S, et al. Semiconductive, flexible MnO_2 NWs/chitosan hydrogels for efficient solar steam generation. ACS Sustainable Chemistry & Engineering, 2021, 9(10): 3887–3900

[11] Xu Y, Lv B, Yang Y, et al. Facile fabrication of low-cost starch-based biohydrogel evaporator for efficient solar steam generation. Desalination, 2021, 517: 115260

[12] Fan Z, Ren J, Bai H, et al. Shape-controlled fabrication of MnO/C hybrid nanoparticle from waste polyester for solar evaporation and thermoelectricity generation. Chemical Engineering Journal, 2023, 451(1): 138534

[13] Hanif Z, Tariq M Z, Khan Z A, et al. Polypyrrole-coated nanocellulose for solar steam generation: a multi-surface photothermal ink with antibacterial and antifouling properties. Carbohydrate Polymers, 2022, 292: 119701

[14] Fan D, Lu Y, Zhang H, et al. Synergy of photocatalysis and photothermal effect in integrated 0D perovskite

oxide/2D MXene heterostructures for simultaneous water purification and solar steam generation. Applied Catalysis B: Environmental, 2021, 295: 120285

[15] Chen Y, Qiu H S, Li X F, et al. Three-level pore structure hydrogels for solar vapor generation. Applied Surface Science, 2022, 582: 152483

[16] Qiu J X, Xu X Y, Li Z, et al. A solar-electric dual-driven microporous hydrogel evaporator for all-weather highly efficient water purification. Nano Energy, 2024, 130: 110057

[17] Yue Y Y, Wang Y, Bai Y, et al. A loofah-based all-day-round solar evaporator with phenolic lignin as the light-absorbing material for a highly efficient photothermal conversion. Chemical Engineering Journal, 2023, 477: 147298

[18] Xu X Y, Zhao Q, Liu Q, et al. Full-spectrum-responsive Ti_4O_7–PVA nanocomposite hydrogel with ultrahigh evaporation rate for efficient solar steam generation. Desalination, 2024, 577: 117400